Advanced Electronic Materials

ADVANCED ELECTRONIC MATERIALS Open Access

www.advelectronicmat.de

RESEARCH ARTICLE OPEN ACCESS

High-Throughput Screening and Characterization of Non-Flammable Na-Cl Solid Electrolytes

Naoto Tanibata[1] | Naoki Nonaka[1] | Daisuke Urushihara[1] | Hayami Takeda[1] | Ryo Kobayashi[2] | Naoaki Kuwata[3] | Masanobu Nakayama[1]

[1]Department of Advanced Ceramics, Nagoya Institute of Technology, Nagoya, Aichi, Japan | [2]Department of Applied Physics, Nagoya Institute of Technology, Nagoya, Aichi, Japan | [3]Research Center for Energy and Environmental Materials (GREEN), National Institute for Materials Science (NIMS), Tsukuba, Ibaraki, Japan

Correspondence: Naoto Tanibata (tanibata.naoto@nitech.ac.jp)

Received: 1 October 2025 | **Revised:** 15 December 2025 | **Accepted:** 7 January 2026

Keywords: all-solid-state batteries | chloride solid electrolytes | ignition temperature | sodium-ion conductivity

ABSTRACT

Non-flammable solid electrolytes are key materials in all-solid-state batteries. Chloride solid electrolytes exhibit high ionic conductivities derived from weak Coulomb interactions with carrier ions. However, not all chlorides are stable, and a limited number of Na-Cl-based materials exhibit ionic conductivities above 10^{-4} S cm^{-1}. Herein, the ionic conductivities of Na-Cl compounds in a structural database (Materials Project) are comprehensively calculated through force field molecular dynamics and density functional theory calculations. The results predict that $Na_3La_5Cl_{18}$ (mp-1173723) is thermodynamically stable with a high ionic conductivity (1.5×10^{-2} S cm^{-1}) at 298 K. Moreover, the 1D conduction pathway along the *c*-axis of $Na_3La_5Cl_{18}$ is confirmed. Nuclear magnetic resonance measurements confirm the high ionic conductivity (>10^{-4} S cm^{-1} at 298 K) of synthesized $Na_3La_5Cl_{18}$. Analysis of characterization results reveals that the ionic conductivity of $Na_3La_5Cl_{18}$ can be further improved by suppressing La mixing in the 1D conduction pathway, while impedance measurements and relaxation time analysis show that conductivity is enhanced by reducing the large crystallite grain boundary resistance. $Na_3La_5Cl_{18}$ has a higher ignition temperature (>800°C) compared to the sulfide electrolyte Na_3PS_4 (~300°C). The results of this study enable the realization of ASSBs with improved safety.

1 | Introduction

The development of high-performance storage batteries with a low environmental impact is required to solve energy and environmental problems [1]. All-solid-state Li batteries using nonflammable solid electrolytes have gained attention in recent years because of their potential for high safety operation and high energy density [2]. All-solid-state Na batteries, in which Li is replaced by the chemically similar and more abundant Na, can reduce the risk associated with resources such as Li [3]. To realize Na-based all-solid-state batteries, a solid electrolyte with high Na-ion conductivity is essential [4]. In addition to high ionic conductivity, solid electrolytes must exhibit high deformability and a wide potential window. Conventional oxide materials have low deformability, and the fabrication of all-solid-state batteries, where charge–discharge reactions occur at the solid-solid interface, generally involves sintering at high temperatures [5]. The sintering process can cause the volatilization of the constituent elements and induce side reactions between the electrode and electrolyte. These limitations significantly restrict the number of suitable materials [6]. In Li systems, chloride electrolytes that satisfy all these properties have been recently reported and explored [7]. Chloride systems are expected to exhibit high ionic conductivity and deformability due to the high

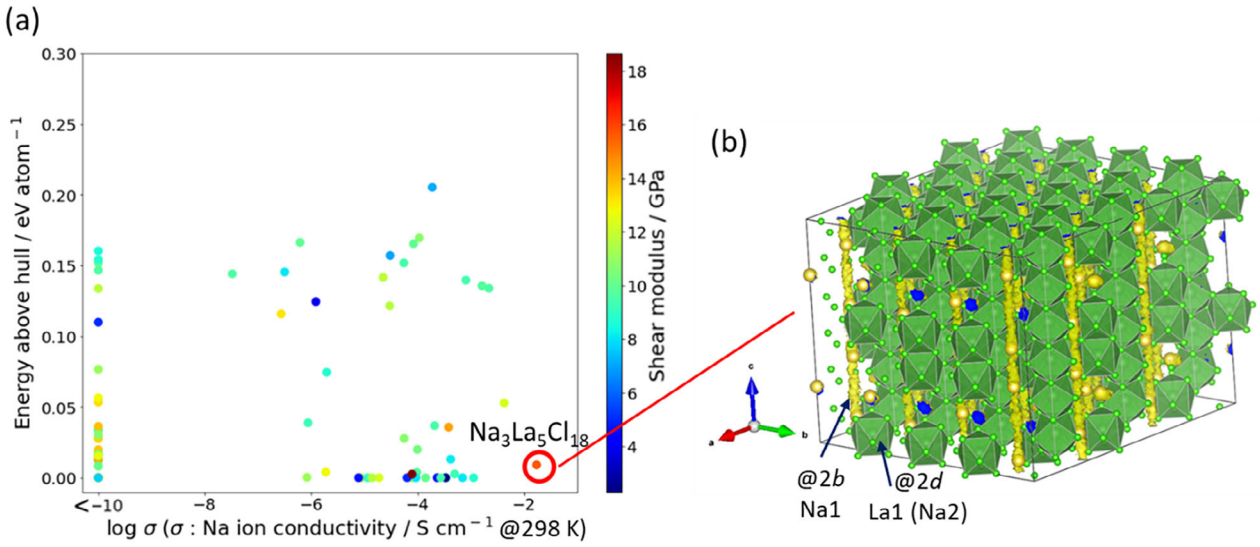

FIGURE 1 | (a) Comprehensive calculation results of three parameters (Na ion conductivity σ at 298 K, energy above hull, and shear modulus) for Na-Cl materials in the structure database (Materials Project). Materials in which Na did not diffuse during molecular dynamic calculations are plotted as having a low ionic conductivity with $\sigma = 10^{-10}$ S cm^{-1} as the lower limit. (b) Trajectory of Na ions during molecular dynamic calculations for $Na_3La_5Cl_{18}$, which is suggested to be a high ionic conductor.

polarization and low charge density of chloride ions, which result in low interactions with counter cations. However, not all chloride materials exhibit high ionic conductivity and deformability, and the Na-Cl systems that have been investigated so far have conductivities that are lower than those of Li-Cl systems. Room temperature ionic conductivities above 10^{-4} S cm^{-1} have been reported for Li-Cl-based crystals [8], while Na-Cl-based crystals have room temperature ionic conductivities below 1×10^{-4} S cm^{-1}. Specifically, the ionic conductivities are 3.9×10^{-6} S cm^{-1} for $NaAlCl_4$ [9]; 1.8×10^{-5} S cm^{-1} for Na_2ZrCl_6 [10]; 6.6×10^{-5} S cm^{-1} for $Na_{2.25}Y_{0.25}Zr_{0.75}Cl_6$ [11]; 6.2×10^{-5} S cm^{-1} for $NaTaCl_6$ [12]; and 1×10^{-4} S cm^{-1} for $Na_{1.1}Ta_{0.9}Zr_{0.1}Cl_6$ [13].

In this study, promising Na-Cl-based ionic conductors were exhaustively explored through the computational screening of compounds in a structural database (Materials Project) [14]. The ionic conductivity of the electrolyte was determined through molecular dynamics using a high-throughput force field (FF) [15], in which the FF parameter sets were derived from short density functional theory-molecular dynamics (DFT-MD) simulations (2 ps simulation time). It has been established that the shear modulus is a good indicator of deformability in Li systems, which was also observed in the present study using density functional perturbation theory [16]. Furthermore, to increase synthesizability, we also considered the energy above the hull (the energetic distance above the convex hull, which is formed by the energetically lowest states) in the Materials Project database and selected materials for experimental investigation. Then, the flammability of the selected Na-Cl electrolyte, which is one factor that significantly influences the safety of the all-solid-state batteries, is evaluated by ignition and flash tests.

2 | Results and Discussion

The computational screening results for the NaCl compounds are shown in Figure 1a. While Na does not diffuse in many materials (plotted at $\sigma = 10^{-10}$ S cm^{-1} as the lower limit), $Na_3La_5Cl_{18}$ (mp-1173723) showed a high ionic conductivity (1.5×10^{-2} S cm^{-1}) at 298 K, which is comparable to that of organic liquid electrolytes. The shear modulus is relatively large (16 GPa) in the NaCl system, suggesting that low deformability with a large grain boundary resistance may be an issue. $Na_3La_5Cl_{18}$ is of interest in this study because it also has a relatively small energy above the hull (0.0091 eV atom^{-1}), which indicates that it is thermodynamically stable. Information on the other materials is summarized in Table S1. $Na_3La_5Cl_{18}$ has a $LaCl_8$ polyhedron that forms a 1D tunnelling pillar structure with Na ions in the tunnel and pillar. High-precision first-principles DFT-MD calculations were performed on this material at 900 K. The mean square distance (MSD) values of the DFT-MD calculations are shown in Figure S1a, where only Na was diffused. In addition, the MSD profiles of Na ions decomposed into the *a*-, *b*-, and *c*-axis components (Figure S1b) and Na trajectory during molecular dynamics calculations (Figure S1c–e) indicates a clear 1D conduction path along the *c*-axis, similar to the trajectory of Na during molecular dynamics calculations using the high-throughput screening force field, as shown in Figure 1b.

$Na_3La_5Cl_{18}$ was calculated to have a low decomposition energy and was synthesized through a solid-state reaction following previous reports [17]. Powder X-ray diffraction (XRD) patterns (Figure 2) show that the raw material peaks disappeared and a single phase of monoclinic $Na_3La_5Cl_{18}$ was obtained. The Rietveld analysis results based on Inorganic Crystal Structure Database (ICSD) structures (ICSD No. 74923, *S.G.*: $P\,6_3/m$) [20] are presented in Figure 2 and Table 1. In the optimized and validated structure (R_{wp} = 5.34%, R_B = 7.73%, R_F = 3.92%, S = 1.34), the La atom, which was supposed to be at the 2*d* site, was found at the 2*b* site of the Na^+ conduction pathway by approximately 4%. The structure was also found to contain approximately 10% less Na at the 2*b* sites and 10% more Na at the 2*d* La sites. These results suggest that some cation mixing occurred between Na^+ and La^{3+} with close ionic radii

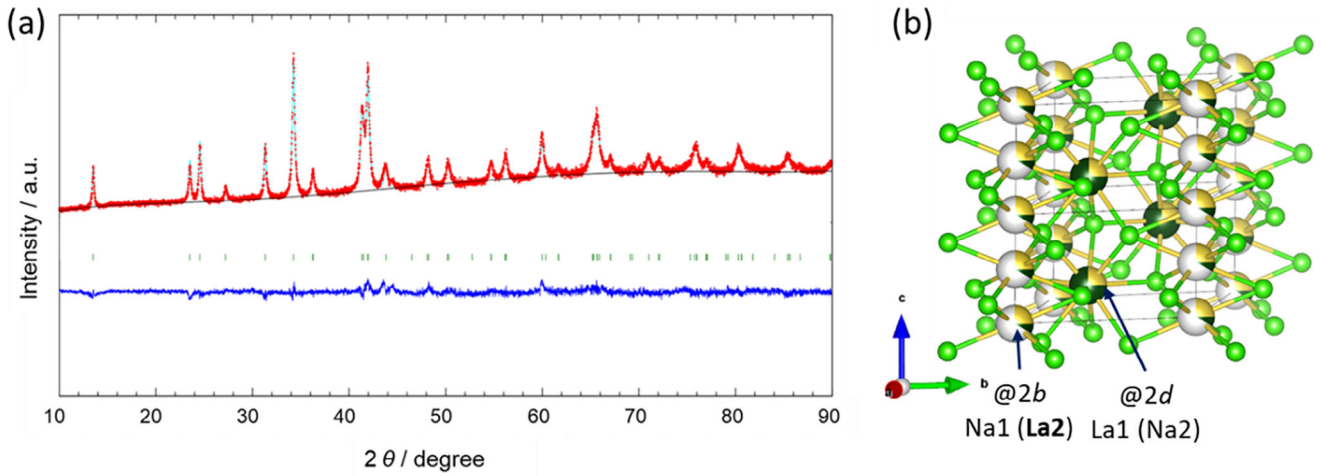

FIGURE 2 | (a) Rietveld refinement XRD pattern for the synthesized $Na_3La_5Cl_{18}$ particles. (b) Adapted crystal structure model.

TABLE 1 | Structural parameters after Rietveld refinement.

Atom	Site	g	x	y	z	B(Å²)
Na1	2b	0.300(-)	0	0	0	1.0
Na2	2d	0.200(-)	2/3	1/3	1/4	1.0
La1	2d	0.800(3)	2/3	1/3	1/4	1.0
La2	2b	0.033(-)	0	0	0	1.0
Cl1	6h	1	0.0832(4)	0.3850(5)	1/4	1.0

S.G.: $P\,6_3/m$ (176).
Lattice parameter (Å): $a = 7.571(2)$, $c = 4.3540(7)$.
Reliability factors: $R_{wp} = 5.34$, $R_B = 7.73$, $R_F = 3.92$, $S = 1.34$.

(Na^+: 1.02 nm; 6-coordination, La^{3+}: 1.03 nm; 6-coordination) [18].

The analysis results for the compacted $Na_3La_5Cl_{18}$ samples are shown in Figure 3. The AC impedance plot (Figure 3a) shows a large semicircle and a spike. As the spike was assumed to originate from the ion-blocking electrode, the ionic conductivity was calculated from the size of the semicircle (R_{total}) in the diagram. The calculated ionic conductivity (5.5×10^{-8} S cm^{-1}) is much lower than the value suggested by the MD calculation (1×10^{-2} S cm^{-1}). To investigate the resistive component in more detail, a relaxation time distribution (DRT) analysis [19, 20] was performed on the impedance spectrum. In the DRT spectrum (Figure 3b), two resistive components (DE1 and DE2), consisting of resistance R and time constant T, were detected in addition to resistance R_0 at the intersection with the real axis. Therefore, the fitting was performed using the equivalent circuit shown in the inset. R_0 is a reference value that was fixed at an intermediate stage of the fitting procedure, because the solution did not converge when R_0 was fitted simultaneously with the other resistance components. To determine the resistive components, the capacitance C was calculated using Equation (1).

$$C = \frac{DE - T}{DE - R} \quad (1)$$

where DE-T and DE-R are the relaxation time and resistance of the DE component, respectively. Information on the resistive components is presented in Table 2. The capacitance of DE1, which has a higher resistance, is 2.3×10^{-10} F, whereas the capacitance of DE2 is 7.6×10^{-9} F. The capacitance within the bulk crystallite is approximately 10^{-12} F, based on the dielectric constants of common materials [21]. Furthermore, it is known from the brickwork model that the capacitance at the grain boundaries is proportional to the size of the crystallites, and increases from the capacitance in the crystallite bulk in the ratio of the crystallite size to the thickness of the grain boundary (approximately 10^{-10} m) [21]. The crystallite size was calculated using the Halder–Wagner method (91 nm), and the capacitance of the crystallite grain boundary (C_{cb}), approximated using the Brickwork model, was 10^{-10} F, which corresponds to the capacitance of the first resistive component, DE1. This indicates that DE1 is mainly derived from the crystallite grain boundary. The same concept can also be applied to the capacitance of the particle grain boundary resistance, which is assumed to be larger than the crystallite bulk capacitance based on the ratio of the particle size to the grain boundary thickness. The particle grain boundary capacitance (10^{-8} F) estimated from the particle size (several micrometers) observed in the scanning electron microscopy (SEM) image of the $Na_3La_5Cl_{18}$ powder (Figure S2) is close to the capacitance of the second resistive component DE2 (7.6×10^{-9} F). Therefore, the second resistive component is derived mainly from the particle–grain boundary resistance. The crystallite grain boundary resistance accounted for a significant proportion (84%) of this resistance. One of the factors responsible for this large grain-boundary resistance may be the influence of 1D conduction, as suggested by computational chemistry. The percentage of particle grain boundary resistance to the total grain boundary resistance (where the latter is defined as the sum of the crystallite grain boundary resistance and the particle grain boundary resistance), which is also an indicator of the deformability of the particles, is 16%. To investigate the deformability of the particles, SEM observations of the fractured surfaces of the compacted $Na_3La_5Cl_{18}$ were performed (Figure 3c), revealing many voids between the particles. In addition, the relative density, calculated from the apparent density of the compacted $Na_3La_5Cl_{18}$ powder, and the crystal lattice density of hexagonal $Na_3La_5Cl_{18}$

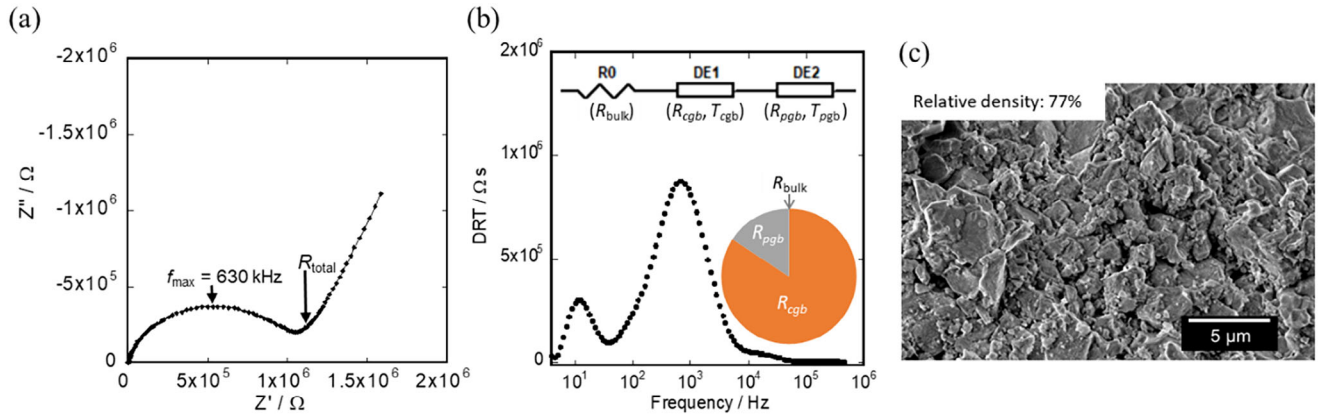

FIGURE 3 | Analytical results for the pressed $Na_3La_5Cl_{18}$ powder. (a) AC impedance plot. (b) DRT spectrum. The inset shows the proposed equivalent circuit model and a pie chart of the resistive component fraction after fitting. R_{bulk}, R_{cgb}, and R_{pgb} correspond to the resistance of the crystalline bulk, crystallite grain boundary, and particle grain boundary, respectively. (c) Fracture surface SEM image of the compacted $Na_3La_5Cl_{18}$ pellet. To reduce charge-up, 10 wt.% Ketjen black was hand mixed.

TABLE 2 | Resistivity analysis results for the $Na_3La_5Cl_{18}$ pellet. The resistance and capacitance obtained from equivalent circuit fitting and the resistance components are listed. R_0 is a reference value that was fixed during the fitting process because it diverged when fitted simultaneously with the parameters of the other resistance components.

Symbol	Resistance / Ω	Capacitance / F	Resistance component
R_0	(585.4)	—	Crystalline bulk resistance R_{bulk}
R_1	9.6×10^5	2.3×10^{-10}	Crystallite grain boundary resistance R_{cgb}
R_2	1.8×10^5	7.6×10^{-9}	Particle grain boundary resistance R_{pgb}

(3.54 g cm^{-3}) is low (77%). However, necks formed between the grains, which may explain the relatively low grain boundary resistance. These deformability values (relative density and particle resistance ratio) are consistent with the relationship between the shear modulus and deformability suggested for the Li system, as shown in Figure S2. Therefore, the relationship between the shear modulus and deformability of the Li system may be applicable to the Na system. Because this material is prone to developing strong texturing due to its tunnel-type structure, press treatments under high-temperature or high-pressure conditions are not necessarily appropriate. Nevertheless, we believe that systematically examining these processing conditions in future studies will further deepen the above discussion on the separation of grain-boundary resistances.

The ionic conductivity of the crystallite bulk is calculated to be 1.5×10^{-4} S cm^{-1} from the resistance of R_0. To confirm this ionic conductivity, 23Na-NMR measurements were also performed. In the 23Na-NMR spectrum shown in Figure 4a, a peak with a shoulder was observed with a chemical shift around -15 ppm. Peak separation of this peak using the forked function revealed a large peak on the high field side (signal 1) and a small peak on the low field side (signal 2). There are two Na sites in $Na_3La_5Cl_{18}$, 2*b* and 2*d*, and that their site ratio is $2b : 2d = 2 : 1$. From this, signal 1 with a high integrated intensity was attributed to Na at the 2*b* site and signal 2 with a low integrated intensity was attributed to Na at the 2*d* site. The integrated intensities for these two peaks was calculated to be 53 : 47 for signal 1 and signal 2, indicating that the proportion of La mixing with Na sites in the Na^+ conduction pathway is similar (~7.8%) to that of the Rietveld analysis (~6.0%). The temperature dependences of the half-widths of the ^{23}Na-NMR spectra are shown in Figure S4, indicating a conductor-specific motional narrowing. Motional narrowing is known to occur in non-diffusing atoms because of the diffusing atoms [22], and the half-width of the nonconducting site at site 2*d* is assumed to be reduced by the diffusion of Na at site 2*b*, which is diffused in the MD calculations shown in Figure 2. If the half-width is ΔW, the activation energy of ionic conduction, E_a, can be determined by Equation (2) [23]:

$$\Delta W_0 = Aexp\left(\frac{E_a}{kT}\right) + \Delta W \tag{2}$$

where k is the Boltzmann's constant, A is a constant in the pre-exponential factor, and ΔW_0 is the width at half-maximum at 303 K. Consequently, the diffusion activation energy of the 2*b* site on the conduction path was as low as 0.30 eV. The ionic conductivity was then determined by measuring the spin-lattice relaxation time T_1 for the conduction-site-derived signal 1. T_1 was measured at each temperature using the saturation recovery method described in Equation (3) [24].

$$M_z(\tau) = M_0\left\{1 - \exp\left(-\frac{\tau}{T_1}\right)\right\} \tag{3}$$

where $M_z(\tau)$ is the nuclear magnetization in the same direction as the external magnetic field and τ is the saturation recovery time. The inverse of the spin-lattice relaxation time T_1^{-1} shown in

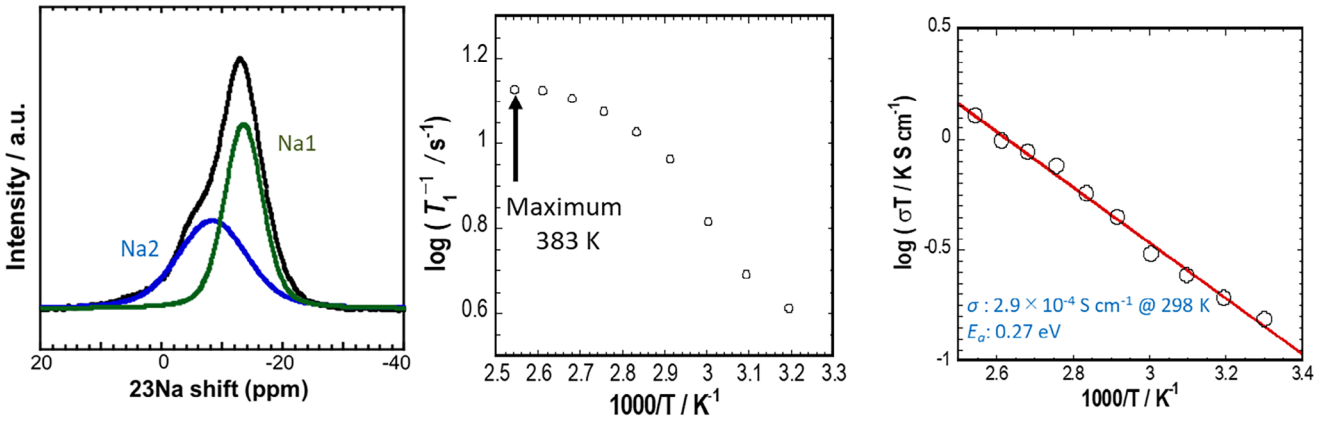

FIGURE 4 | ^{23}Na-MAS NMR measurements. (a) NMR spectra. (b) Temperature dependence of the spin-lattice relaxation time T_1^{-1}. (c) Arrhenius plot of ionic conductivity obtained from the spin-lattice relaxation time.

Figure 4b reaches a maximum in its temperature dependence at $T = 383$ K. The molecular correlation time, τ_c, can be calculated using Equation (4) from the Bloembergen-Purcell-Pound (BPP) theory [25, 26], which explains the contribution of T_1^{-1} to ion dynamics.

$$\frac{1}{T_1} = C\left(\frac{\tau_c}{1+\omega_0^2\tau_c^2} + \frac{4\tau_c}{1+4\omega_0^2\tau_c^2}\right) \tag{4}$$

where ω_0 is the frequency of the external magnetic field, and C is a constant that depends on the relaxation mechanism; $\tau_c = 0.616/\omega_0$ holds at the maximum value of T_1^{-1}, so that T_1 and τ_c have a one-to-one relationship. The τ_c obtained here can be converted into the self-diffusion coefficient D using the Einstein–Smolkowski equation [27] expressed in Equation (5).

$$D = \frac{l^2}{2d\tau_c} \tag{5}$$

where l is the jump distance, and d is the diffusion dimension. In this case, l is the distance between the conduction sites (2*b* sites) of the crystal structure, and d is calculated to be 1 because the material is a 1D conductor. The Nernst–Einstein equation, expressed in Equation (6), calculates the ionic conductivity σ from the diffusion coefficient D.

$$\sigma T = \frac{z^2F^2c}{R}D \tag{6}$$

where z is the ionic valence, F is the Faraday constant, c is the density of the carrier Na at the 1D conduction site, R is the gas constant, and T is the absolute temperature. An Arrhenius plot of the ionic conductivity obtained from the spin-lattice relaxation time shown in Figure 4c gives an ionic conductivity of 2.9×10^{-4} S cm^{-1} at 298 K and an activation energy of 0.27 eV. This activation energy is in close agreement with the value obtained from the motional narrowing (0.30 eV). This ionic conductivity is comparable to the bulk conductivity (1.5×10^{-4} S cm^{-1}) calculated from the bulk resistance obtained by impedance measurements, supporting that the bulk resistance value fixed during the fitting procedure does not significantly affect the above discussion on grain-boundary resistance. Therefore, we conclude that the primary reason why the ionic conductivity of the pellet estimated from impedance measurements is several orders of magnitude lower than that obtained from MD calculations and NMR measurements is the extremely large grain-boundary resistance. Note that the influence of differences arising from the measurement techniques, such as the Haven ratio [28], is considered to be negligible compared with the more than four orders of magnitude difference observed in this study. On the other hand, the ionic conductivity value is relatively high in the Na-Cl system; however, it was still lower than the ionic conductivity (10^{-2} S cm^{-1}) obtained from the MD simulations. This can be attributed to the fact that the conduction of Na ions occurs in one dimension. In the case of 1D conduction, in addition to a larger grain boundary resistance owing to the anisotropy of conduction, defects such as those suggested by NMR spectroscopy and Rietveld analysis block the conduction pathways and significantly reduce conductivity. A semi-quantitative discussion of the effects of blocking defects on 1D conduction [29] is provided below. In the present material, Rietveld refinement reveals that approximately 3.3% of the Na^+ conduction sites (2*b*) are occupied by immobile multivalent La^{3+} ions. The average crystallite size is 91 nm, and considering a *c*-axis lattice parameter of 4.3540 Å and two 2*b* sites per unit cell, approximately 418 Na^+ conduction sites are estimated to be continuously aligned along a single 1D conduction channel. With 3.3% of these sites blocked by La^{3+}, each 1D conduction channel is estimated to contain, on average, approximately 13.8 La^{3+}-induced blocking defects randomly distributed along the channel. As a result of this random distribution of more than ten blocking defects, the probability of forming a continuous 1D superionic conduction pathway over long distances becomes extremely low, and the conduction pathway is effectively fragmented into short segments. Consequently, in contrast to the local superionic diffusion behavior predicted by MD simulations for an ideal, defect-free structure, the ionic conductivity experimentally observed in real materials is thought to be strongly limited by such pathway fragmentation. Therefore, in future studies, synthesis with the suppression of defect formation and an increase in conduction pathways by elemental substitution will be performed, and the superionic conductivity suggested by MD simulations will be measured.

Finally, the flammability of the chloride electrolyte, which determines the safety of all-solid-state batteries, was evaluated and compared to that of a typical sulfide solid electrolyte (Na_3PS_4

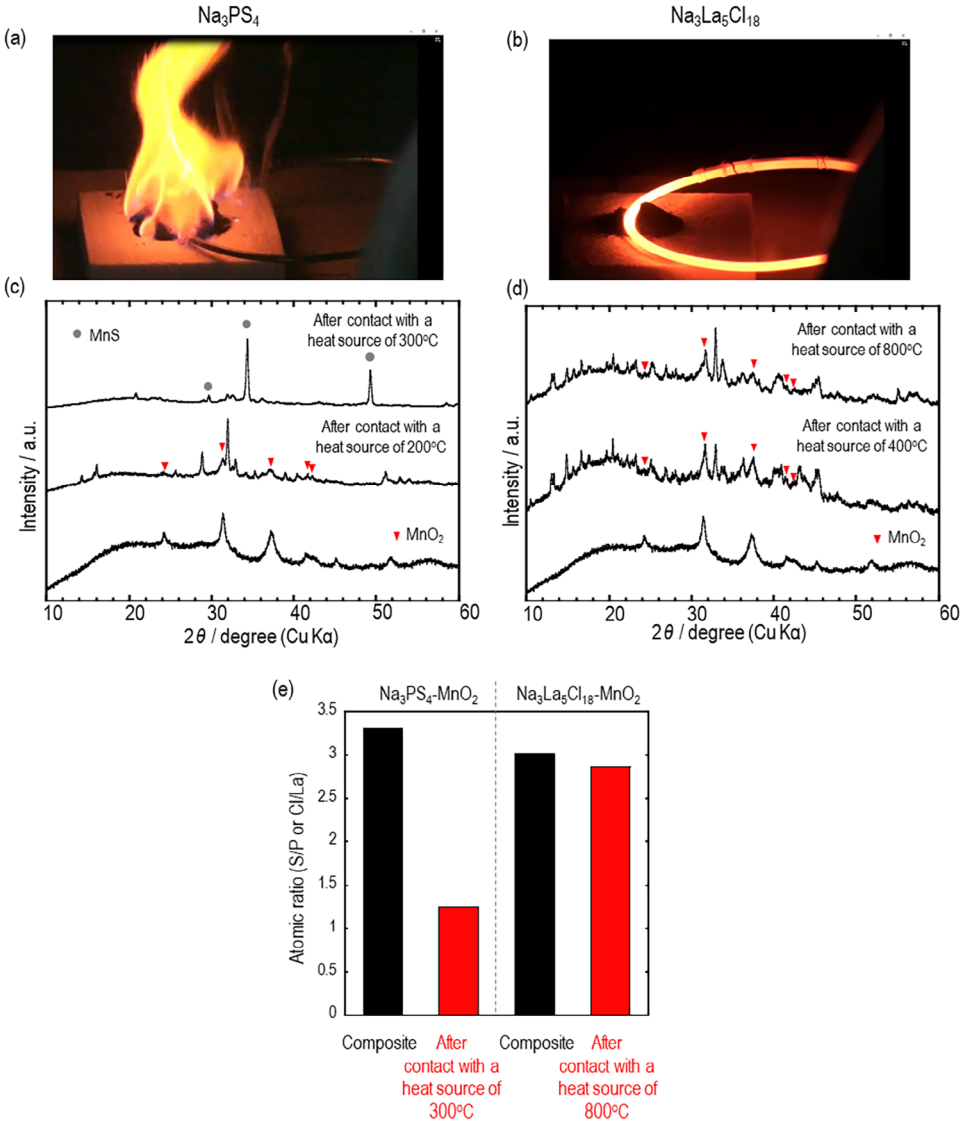

FIGURE 5 | Ignition test results. Photograph of (a) Na_3PS_4 powder in contact with a heat source at 300°C and (b) $Na_3La_5Cl_{18}$ powder in contact with a heat source at 800°C. XRD patterns before and after the ignition test for (c) Na_3PS_4 powder and (d) $Na_3La_5Cl_{18}$ powder. (e) Elemental ratios determined by EDS of Na_3PS_4 and $Na_3La_5Cl_{18}$ powders before and after the ignition test.

glass-ceramic). As shown in Figure 5a,b, $Na_3La_5Cl_{18}$ does not ignite even when in contact with a heat source at 800°C, whereas Na_3PS_4 ignites when the heat source temperature is 300°C. Elemental analysis using energy dispersive X-ray spectroscopy (EDS) before and after the ignition test (Figure 5e) reveals that the ignition test reduced the flammable S component in Na_3PS_4 but not the Cl component in $Na_3La_5Cl_{18}$. Moreover, in the XRD patterns shown in Figure 5c,d, for MnO_2 (the electrode active material in the charged state), it can be observed that in Na_3PS_4 the MnO_2 peak disappears because of the ignition test and the formation of a reduced Mn compound (MnS), while in $Na_3La_5Cl_{18}$ the MnO_2 peak was maintained at 400°C and 800°C. The flash test also confirmed that Na_3PS_4 exhibits the flash phenomenon at 200°C, whereas $Na_3La_5Cl_{18}$ did not ignite, at least up to 300°C. These results show that chloride-based solid electrolytes are not flammable, ensuring the safety of all-solid-state batteries. In future studies, evaluations at higher temperatures, as well as safety comparisons with oxide-based and other chloride-based electrolytes, will be investigated.

3 | Conclusions

Among solid electrolytes, Na-Cl compounds are expected to have high-performance properties (such as high ionic conductivity, high deformability, and high oxidation potential), making them excellent materials for the next generation of Na-based all-solid-state sodium batteries; however, material exploration is still limited. In this study, computational screening was performed for Na-Cl compounds, which suggested the existence of $Na_3La_5Cl_{18}$ with a 1D path of super-ionic conduction ($\sigma_{25} > 10^{-2}$ S cm^{-1}) at 298 K. ^{23}Na-NMR spectroscopy of the as-synthesized sample showed a bulk Na ionic conductivity above 10^{-4} S cm^{-1} at room temperature. This ionic conductivity is high, reported for the Na-Cl system; however, it is lower than the theoretical conductivity determined by molecular dynamics calculations. A possible reason for this is the presence of dilute amounts of La cations in the 1D conduction pathway, as confirmed by NMR spectroscopy and Rietveld analysis. Therefore, higher ionic conductivities can be expected in the future by optimizing

synthesis methods and elemental substitutions. The crystalline grain boundary resistance suggested by impedance measurements and DRT analysis is also expected to improve by enhancing the fabrication conditions and multi-dimensionalization of the conduction pathways. Finally, the chloride electrolyte has a higher ignition temperature than the sulfide electrolyte, indicating that it is an excellent solid electrolyte for realizing nonflammable all-solid-state batteries. In future work, comprehensive battery-level performance evaluations will be considered once improvements in the ionic conductivity of the pelletized samples are confirmed.

4 | Experimental Section

4.1 | Computational Screening for Na-Cl Solid Electrolytes

A total of 86 compounds containing Na–Cl listed in the crystal structure database (Materials Project) [14] were examined. The Na diffusion coefficients were calculated through molecular dynamics simulations using a high-throughput force field (FF-MD) as described in a previous study [15]. Force-field parameters were determined using a metaheuristic algorithm (Cuckoo search) [30] with a density functional theory-molecular dynamics (DFT-MD) dataset. DFT MD simulations were performed at 900 K for 1 ps (1 fs per step). The kinetic energy cut-off was set at 350 eV. Owing to the limited computational resources, 1 × 1 × 1 *k*-point sampling was performed. The energy convergence criterion was set to 10^{-3} eV. Specifically, classical force field parameters were optimized using the Cuckoo search algorithm so as to reproduce structural descriptors obtained from DFT-MD and FF-MD simulations, including the radial distribution function (RDF), angular distribution function (ADF), and lattice parameters. The force field (FF) model employed in this study consists of two-body and three-body potential terms. The two-body potential $U(r_{ij})$, defined by the interatomic distance r_{ij} between particles i and j, is similar to a Bond Valence Sum–based force field (BVS-FF) and is composed of two terms, as shown in Equation (7).

$$U\left(r_{ij}\right) = \frac{1}{4\pi\epsilon 0}\frac{q_i q_j}{r_{ij}}\mathrm{erfc}\left(\frac{r_{ij}}{\rho_{ij}}\right) + D_e\left\{exp\left[-2\alpha\left(r-R_e\right)\right] - 2exp\left[-\alpha\left(r-R_e\right)\right]\right\} \quad (7)$$

The first term represents interactions between like-charged species (anion–anion and cation–cation) and was described by a screened Coulomb potential. The second term accounts for interactions between oppositely charged species (cation–anion) and was represented by a Morse potential. In the screened Coulomb potential, the screening effect was described using the charges $q_i$and q_j together with the error function, and the screening length ρ_{ij} is treated as an optimization parameter. In contrast, for the Morse potential, the equilibrium bond distance R_e, well depth D_e, and the parameter α, which determines the potential width, are used as optimization parameters. For the three-body interactions among particles i, j, and k, the angular-dependent term of the Stillinger–Weber potential (Equation 8) was employed to account for the effects of bond lengths and bond angles.

$$U\left(r_{ijk}\right) = \lambda exp\left[\left(\frac{1}{r_{ij}-r_{cut(3b)}}\right)+\left(\frac{1}{r_{ik}-r_{cut(3b)}}\right)\right]\left(\cos\theta_{ijk}-\gamma\right)^2 \quad (8)$$

here, λ and γ were treated as optimization parameters. To improve computational efficiency, the cutoff distance for the three-body interactions, $r_{\mathrm{cut}(3b)}$, was fixed at 3.5 Å, while the cutoff distance for the two-body interactions, $r_{\mathrm{cut}(2b)}$, was set to 5.0 Å. The mismatch between the RDFs, ADFs, and lattice parameters obtained from DFT-MD and FF-MD simulations was defined as a loss function, which was minimized during the parameter optimization. The final values of the loss function were summarized in Table S1. Although no absolute criterion exists for the loss function value, several samples exhibit loss function values exceeding 0.1, suggesting that the reliability of the corresponding FF parameters was not necessarily high. This may be attributed to limitations or deviations inherent in the classical force field forms defined in Equations (7) and (8). For reference, Figure S5 compares the RDFs of all constituent elements obtained from DFT-MD and FF-MD simulations using the optimized parameters. The Na^+ conductivities were calculated using the Nernst–Einstein equation from the diffusion coefficient obtained from the slope of the MSD in the MD calculation of 298 K using the obtained force field. Furthermore, the shear moduli were calculated using the elastic tensors obtained from the DFT calculations [31]. All force field parameter fitting and molecular dynamics (MD) calculations described above were performed using the Nagoya Atomistic-simulation Package (NAP) [32, 33]. The DFT-based molecular dynamics (DFT-MD) calculations were carried out using the Vienna Ab initio Simulation Package (VASP) [34].

4.2 | Theoretical Evaluation of $Na_3La_5Cl_{18}$

Na diffusivity was evaluated using first-principles MD calculations for $Na_3La_5Cl_{18}$, which was suggested to be a high-Na-ion conductor using classical force-field calculation screening. In addition, the loss function value for the optimized FF parameters of the $Na_3La_5Cl_{18}$ material was 0.06, indicating that the structural features observed in the RDF (Figure S5) were reproduced relatively well. DFT MD simulations were performed at 900 K for 1 ns (1 fs per step). The kinetic energy cut-off was set at 350 eV. Owing to the limited computational resources, 1 × 1 × 1 *k*-point sampling was performed. The energy convergence criterion was set to 10^{-3} eV.

4.3 | Synthesis

$Na_3La_5Cl_{18}$ was synthesized from NaCl (Wako Pure Chemical Industries, Ltd., 99.5%) and $LaCl_3$ powders (Thermo Scientific Chemicals, 99.9%) through a solid-state reaction. A mixture of stoichiometric ratios was placed in a 45 mL stainless steel pot with 10 ZrO_2 balls (10 mm in diameter) and milled with a planetary ball mill apparatus (Fritsch Japan Co., Ltd., P-7 classic line) at a rotation speed of 500 rpm for 4 h. The samples were then pressed into pellets at 30 kN in a glove box in an Ar atmosphere following

the published ICSD protocol, vacuum sealed in Pyrex tubes, and heated in a tube furnace at 500°C for two weeks.

4.4 | Characterization

The $Na_3La_5Cl_{18}$ powder was identified using XRD (Philips X'pert Pro α1). The characteristic X-rays generated by a Cu tube were monochromatized to $K\alpha$1 lines using a pre-mounted monochromator and measured in a fast scan with a 1D semiconductor detector. The measured voltage and current were 45 kV and 40 mA, respectively. The scan step and speed were 0.013° and 0.57° min^{-1}, respectively. Samples were placed in airtight holders and measured in an Ar atmosphere. To perform AC impedance measurements, pellets of the prepared powder samples were prepared. $Na_3La_5Cl_{18}$ powder was placed in a cylindrical polycarbonate with a 10 mm inner diameter, sandwiched between stainless steel as ion-blocking electrodes, and pressurized to 30 kN using a hydraulic press. The AC impedance measurements were performed at an applied voltage of 300 mV in a frequency range of 10^2–10^6 Hz; Z-Assist software (TOYO Co.) was used for the DRT analysis. The fractured surfaces of the compacts were examined using an electron microscope (JSM-6360LV, JEOL, Ltd.) at an acceleration voltage of 10 kV. To investigate the local structure and ion dynamics of the synthesized samples on short-range scales, the chemical shifts and spin-lattice relaxation times of ^{23}Na nuclei were measured in the temperature range of 298–423 K using an NMR spectrometer (JEOL RESONANCE: ECA600II). The external magnetic field was 14.1 T, and the relaxation time was measured at eight points divided by a logarithmic ratio between 0.001 and 2 s. All of the above measurements were performed under an Ar atmosphere.

4.5 | Ignition Tests

An oxidizing agent (MnO_2) simulating the charged state of the cathode was mixed in a mortar with various electrolytes ($Na_3La_5Cl_{18}$ and Na_3PS_4) in a weight ratio of 1:1 and brought into contact with the heat source, a nichrome wire, for up to 60 s. Measurements were performed in air, at a temperature of 11°C and a humidity of 37% (dew point approximately 3°C). The nichrome wire was 10 mm thick, and the sample was set at approximately 0.5 mL. A flash test was also performed according to the JIS standards.

Acknowledgements

This work was partially supported by Grants-in-Aid for Scientific Research (Grant Numbers 24K01157, 24K17755, 24H02203, and 25H01973) from the Ministry of Education, Culture, Sports, Science, and Technology (MEXT), Japan; a CREST grant from the Japan Science and Technology Agency, Japan (Grant Number JPMJCR21O6); and the Data Creation and Utilization-Type Material Research and Development Project (Grant Number JPMXP1122712807) from MEXT. The authors thank Editage for editing and reviewing the manuscript for the English language. Figures illustrating the crystal structures were drawn using the Visualization for Electronic Structural Analysis (VESTA) software (National Institute for Materials Science, Tsukuba, Japan) [35].

Funding

This work was partially supported by Grants-in-Aid for Scientific Research (Grant Numbers 24K01157, 24K17755, 24H02203, and 25H01973) from the Ministry of Education, Culture, Sports, Science, and Technology (MEXT), Japan; a CREST grant from the Japan Science and Technology Agency, Japan (Grant Number JPMJCR21O6); and the Data Creation and Utilization-Type Material Research and Development Project (Grant number: JPMXP1122712807) from MEXT.

Conflicts of Interest

The authors declare no conflicts of interest.

Data Availability Statement

The data that support the findings of this study are available from the corresponding author upon reasonable request.

References

1. B. Dunn, H. Kamath, and J.-M. Tarascon, "Electrical Energy Storage for the Grid: A Battery of Choices," *Science* 334 (2011): 928–935, https://doi.org/10.1126/science.1212741.

2. J. Janek and W. G. Zeier, *A Solid Future For Battery Development* (Nature Publishing Group, 2016): 16141.

3. N. Yabuuchi, K. Kubota, M. Dahbi, and S. Komaba, "Research Development on Sodium-Ion Batteries," *Chemical Reviews* 114 (2014): 11636–11682, https://doi.org/10.1021/cr500192f.

4. S. Lou, F. Zhang, C. Fu, et al., "Interface Issues and Challenges in All-Solid-State Batteries: Lithium, Sodium, and Beyond," *Advanced Materials* 33 (2021): 2000721, https://doi.org/10.1002/adma.202000721.

5. V. Thangadurai, S. Narayanan, and D. Pinzaru, "Garnet-Type Solid-State Fast Li Ion Conductors For Li Batteries: Critical Review," *Chemical Society Reviews* 43 (2014): 4714–4727.

6. S. Wang, Y. Zhang, X. Zhang, et al., "High-Conductivity Argyrodite Li_6PS_5Cl Solid Electrolytes Prepared via Optimized Sintering Processes for All-Solid-State Lithium–Sulfur Batteries," *ACS Applied Materials & Interfaces* 10 (2018): 42279–42285, https://doi.org/10.1021/acsami.8b15121.

7. Y. Nikodimos, W. Su, and B. J. Hwang, "Halide Solid-State Electrolytes: Stability and Application for High Voltage All-Solid-State Li Batteries," *Advanced Energy Materials* 13 (2023): 2202854–2202890, https://doi.org/10.1002/aenm.202202854.

8. B. He, F. Zhang, Y. Xin, et al., "Halogen Chemistry Of Solid Electrolytes In All-Solid-State Batteries," *Nature Reviews Chemistry* 7 (2023): 826–842, https://doi.org/10.1038/s41570-023-00541-7.

9. J. Park, J. P. Son, W. Ko, et al., "$NaAlCl_4$: New Halide Solid Electrolyte for 3 V Stable Cost-Effective All-Solid-State Na-Ion Batteries," *ACS Energy Letters* 7 (2022): 3293–3301, https://doi.org/10.1021/acsenergylett.2c01514.

10. H. Kwak, J. Lyoo, J. Park, et al., "Na_2ZrCl_6 Enabling Highly Stable 3 V All-Solid-State Na-Ion Batteries," *Energy Storage Materials* 37 (2021): 47–54, https://doi.org/10.1016/j.ensm.2021.01.026.

11. E. A. Wu, S. Banerjee, H. Tang, et al., "A Stable Cathode-Solid Electrolyte Composite For High-Voltage, Long-Cycle-Life Solid-State Sodium-Ion Batteries," *Nature Communications* 12 (2021): 1256, https://doi.org/10.1038/s41467-021-21488-7.

12. K. Motohashi, H. Tsukasaki, A. Sakuda, S. Mori, and A. Hayashi, "$NaTaCl_6$: Chloride as the End-Member of Sodium-Ion Conductors," *ACS Materials Letters* 6 (2024): 1178–1183, https://doi.org/10.1021/acsmaterialslett.3c01445.

13. Z. Huang, S. Yoshida, H. Akamatsu, K. Hayashi, and S. Ohno, "$NaMCl_6$ (M = Nb and Ta): A New Class of Sodium-Conducting Halide-Based Solid Electrolytes," *ACS Materials Letters* 6 (2024): 1732–1738, https://doi.org/10.1021/acsmaterialslett.4c00315.

14. A. Jain, S. P. Ong, G. Hautier, et al., "Commentary: The Materials Project: A Materials Genome Approach To Accelerating Materials Innovation," *APL Mater* 1 (2013): 011002.

15. R. Kobayashi, "nap: A Molecular Dynamics Package With Parameter-Optimization Programs For Classical And Machine-Learning Potentials," *Journal of Open Source Software* 6 (2021): 2768, https://doi.org/10.21105/joss.02768.

16. N. Tanibata, S. Aizu, M. Koga, et al., "Guidelines For Designing High-Deformability Materials For All-Solid-State Lithium-Ion Batteries," *Journal of Materials Chemistry A* 12 (2024): 15601, https://doi.org/10.1039/D4TA02328E.

17. H. J. Seifert, "Ternary Chlorides of the Trivalent Late Lanthanides: Phase Diagrams, Crystal Structures and Thermodynamic Properties," *J Therm Anal Calorim* 83 (2006): 479–505, https://doi.org/10.1007/s10973-005-7132-7.

18. R. D. Shannon, "Revised Effective Ionic Radii and Systematic Studies of Interatomic Distances in Halides and Chalcogenides," *Acta Crystallographica Section A* 32 (1976): 751–767, https://doi.org/10.1107/S0567739476001551.

19. N. Tanibata, S. Takimoto, and K. Nakano, et al., "Metastable Chloride Solid Electrolyte with High Formability for Rechargeable All-Solid-State Lithium Metal Batteries," *ACS Mater Lett* 2 880–886, https://doi.org/10.1021/acsmaterialslett.0c00127.

20. H. Sumi, H. Shimada, Y. Yamaguchi, et al., "Degradation Evaluation by Distribution of Relaxation Times Analysis for Microtubular Solid Oxide Fuel Cells," *Electrochim Acta* 339 (2020): 135913, https://doi.org/10.1016/j.electacta.2020.135913.

21. J. T. S. Irvine, D. C. Sinclair, and A. R. West, "Electroceramics: Characterization by Impedance Spectroscopy," *Advanced Materials* 2 (1990): 132–138, https://doi.org/10.1002/adma.19900020304.

22. A. Dorai, S. Kim, N. Kuwata, et al., "Understanding Ion Dynamics in Closoborate-Type Lithium-Ion Conductors on Different Time-Scales," *The Journal of Physical Chemistry Letters* 15 (2024): 4864–4871, https://doi.org/10.1021/acs.jpclett.4c00754.

23. J. R. Hendrickson and P. J. Bray, "A Phenomenological Equation For NMR Motional Narrowing In Solids," *Journal of Magnetic Resonance (1969)* 9 (1973): 341–357, https://doi.org/10.1016/0022-2364(73)90176-5.

24. P. Heitjans, A. Schirmer, and S. Indris, "NMR and β-NMR Studies of Diffusion in Interface-Dominated and Disordered Solids," *Diffusion In Condensed Matter: Methods, Materials, Models* (Springer, 2005): 367–415, https://doi.org/10.1007/3-540-30970-5_9.

25. N. Bloembergen, E. M. Purcell, and R. V. Pound, "Relaxation Effects in Nuclear Magnetic Resonance Absorption," *Physical Review* 73 (1948): 679, https://doi.org/10.1103/PhysRev.73.679.

26. G. Hasegawa, N. Kuwata, K. Hashi, et al., "Lithium-Ion Diffusion in Perovskite-Type Solid Electrolyte Lithium Lanthanum Titanate Revealed by Pulsed-Field Gradient Nuclear Magnetic Resonance," *Chemistry of Materials* 35 (2023): 3815–3824, https://doi.org/10.1021/acs.chemmater.2c03340.

27. A. Einstein, "Über die von der molekularkinetischen Theorie der Wärme geforderte Bewegung von in ruhenden Flüssigkeiten suspendierten Teilchen [AdP 17, 549 (1905)]," *Annalen der Physik* 517 (2005): 182–193, https://doi.org/10.1002/andp.200590005.

28. G. MURCH, "The Haven Ratio in Fast Ionic Conductors," *Solid State Ion* 7 (1982): 177–198, https://doi.org/10.1016/0167-2738(82)90050-9.

29. R. Malik, D. Burch, M. Bazant, and G. Ceder, "Particle Size Dependence of the Ionic Diffusivity", *Nano Lett* 10 (2010): 41234127, https://doi.org/10.1021/nl1023595.

30. X. S. Yang and S. Deb, "Cuckoo Search: Recent Advances and Applications", *Neural Comput Appl* 24 (2014): 169–174.

31. S. Aizu, S. Takimoto, N. Tanibata, et al., "Screening Chloride Li-ion Conductors Using High-Throughput Force-Field Molecular Dynamics," *Journal of the American Ceramic Society* 106 (2023): 30353044, https://doi.org/10.1111/jace.18991.

32. R. Kobayashi, et al., "nap: A Molecular Dynamics Package With Parameter-Optimization Programs for Classical and Machine-Learning Potentials," *J Open Source Softw* 6 (2021): 2768, https://doi.org/10.21105/joss.02768.

33. R. Kobayashi, Y. Miyaji, K. Nakano, and M. Nakayama, "High-Throughput Production of Force-Fields for Solid-State Electrolyte Materials," *APL Mater* 8 (2020):, https://doi.org/10.1063/5.0015373.

34. G. Kresse and J. Furthmüller, "Efficient Iterative Schemes for ab Initio Total-Energy Calculations Using a Plane-Wave Basis set", *Phys Rev B Condens Matter Mater Phys* 54 (1996): 11169–11186, https://doi.org/10.1103/PhysRevB.54.11169.

35. K. Momma and F. Izumi, "VESTA: A Three-Dimensional Visualization System For Electronic And Structural Analysis," *Journal of Applied Crystallography* 41 (2008): 653–658, https://doi.org/10.1107/S0021889808012016.

Supporting Information

Additional supporting information can be found online in the Supporting Information section.

Supporting File: aelm70277-sup-0001-SuppMat 1.docx.